ACS APPLIED ELECTRONIC MATERIALS

pubs.acs.org/acsaelm Article

# Role of Grain Size on Magnon and Phonon Thermal Transport in the Spin Ladder Compound $Ca_9La_5Cu_{24}O_{41}$

Shuchen Li,[§] Shucheng Guo,[§] Youming Xu, Jianshi Zhou, and Xi Chen*

Cite This: *ACS Appl. Electron. Mater.* 2022, 4, 787−794 Read Online

ACCESS | Metrics & More | Article Recommendations | Supporting Information

**ABSTRACT:** The antiferromagnetic spin ladder compound $Ca_9La_5Cu_{24}O_{41}$ is a promising material for thermal management applications due to its largest magnon thermal conductivity near room temperature among all magnetic materials. It remains elusive how boundary and defect scattering processes affect the magnon and phonon thermal transport in this material. Here, we report the thermal transport investigation of $Ca_9La_5Cu_{24}O_{41}$ polycrystals with different grain sizes as compared with single crystals. The thermal conductivity measurements reveal the contrasting role of size effects on magnon and phonon transport. As the average grain size decreases from 4.2 to 0.83 $\mu$m, the lattice thermal conductivity of polycrystalline $Ca_9La_5Cu_{24}O_{41}$ below about 100 K is significantly suppressed, due to the enhanced phonon-boundary scattering. In comparison, the magnon thermal transport is less affected by grain size. According to kinetic model analysis, the magnon mean free paths of two polycrystals are found to be much smaller than the single-crystal values, which is attributed to the magnon-defect scattering instead of magnon-boundary scattering. The obtained magnon mean free path of about 65 Å near 100 K is comparable to the lattice constant of the unit cell along the spin ladder direction, suggesting possible magnon localization in the disordered polycrystalline samples. These results offer useful insights into the development of magnetic materials for spin caloritronic and thermal management applications.

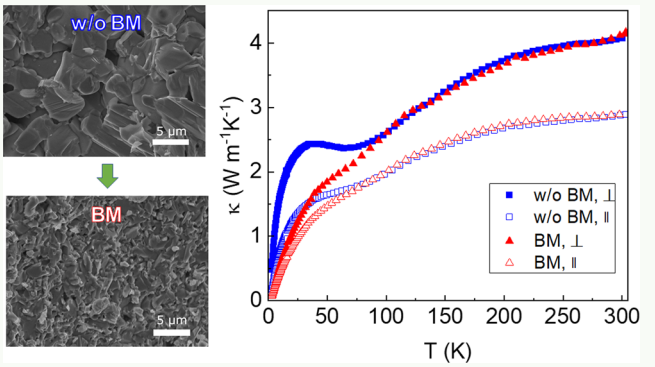


**KEYWORDS:** *thermal conductivity, spin ladder compound, phonons, magnons, localization, grain size, defects*

## INTRODUCTION

Materials with high thermal conductivity ($\kappa$) are needed for the thermal management of electronic devices since heat dissipation is a major challenge that limits device performance.[1−3] Traditionally, materials with large electronic thermal conductivity ($\kappa_E$), such as silver and copper,[4] or large phonon contribution ($\kappa_L$), such as diamond and graphite,[5] have been developed as heat sink materials for microelectronics. Recently, cubic BAs has been found to exhibit an ultrahigh $\kappa$ comparable to diamond due to its unique phonon structure.[6−8] Besides the thermal transport mediated by phonons and electrons, the studies on some magnetic materials indicate a new path to high-$\kappa$ materials through magnetic excitations. The heat transport via magnetic excitations was first predicted in 1936[9] and confirmed experimentally in the yttrium iron garnet in 1962.[10] In the past decade, experimental discoveries of large magnetic thermal conductivity ($\kappa_M$) in low-dimensional antiferromagnetic cuprates draw increasing attention in this field.[11−14] Examples of these cuprates include one-dimensional (1D) spin-chain structure $Ca_2CuO_3$[15] and $Sr_2CuO_3$,[16] spin ladder structure $(Sr,Ca,La)_{14}Cu_{24}O_{41}$,[13,14] and two-dimensional (2D) square lattice structure $La_2CuO_4$.[17] These low-dimensional cuprates usually have the 180° Cu−O−Cu bond configuration that facilitates a large antiferromagnetic interaction ($J$) and magnon group velocity.

Spin ladder compounds $(Sr,Ca,La)_{14}Cu_{24}O_{41}$ exhibit 1D heat transport mediated by magnons. Inelastic neutron scattering studies show that these materials have a strong antiferromagnetic interaction of $J \approx 2000$ K along the ladder direction.[18,19] Previous thermal conductivity measurements have revealed an additional broad $\kappa$ peak with a maximum value over 90 W m$^{-1}$ K$^{-1}$ near 140 K along the spin ladder direction.[14] Below 50 K, thermal transport is dominated by phonons since the magnons are not excited due to the large magnon energy gap of about 32 meV.[18] In addition, the electronic band gap of the compounds is about 2 eV.[20] The electronic thermal conductivity is negligible due to their low electrical conductivity.[21]

**Received:** November 21, 2021
**Accepted:** January 16, 2022
**Published:** January 27, 2022

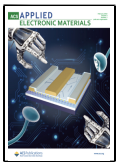

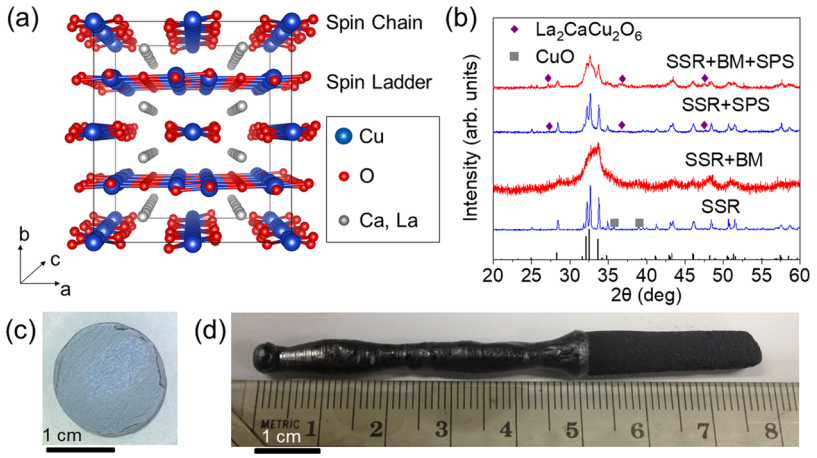


**Figure 1.** (a) Crystal structure of $Ca_9La_5Cu_{24}O_{41}$ based on the data reported by Siegrist et al.[38] (b) XRD patterns of $Ca_9La_5Cu_{24}O_{41}$ samples after SSR, BM, and SPS. (c) Photograph of a $Ca_9La_5Cu_{24}O_{41}$ pellet prepared by SPS. (d) Photograph of a $Ca_9La_5Cu_{24}O_{41}$ ingot grown by the traveling solvent floating zone method.

Experimental efforts have been devoted to understanding the scattering of magnons by mobile holes in spin ladder single crystals. Since the nominal valence of Cu in $Sr_{14}Cu_{24}O_{41}$ is +2.25, some holes are doped in the spin ladders intrinsically. According to the X-ray absorption spectroscopy measurements, there are 6 holes in the chain sublattice and 1 hole in the ladder sublattice per formula unit.[22] These holes can be treated as magnetic defects, which reduce $\kappa_M$. Ca has the same valence state as Sr. However, an increase of the Ca doping level transfers holes from the chains to the ladders,[23] leading to a large suppression of $\kappa_M$ in $Sr_{14-x}Ca_xCu_{24}O_{41}$.[12] On the other hand, when Ca or Sr is replaced by La in $(Sr,Ca)_{14-y}La_yCu_{24}O_{41}$, the hole doping level in ladders drops drastically with the increasing $y$ value. With a nearly hole-free structure, $Ca_9La_5Cu_{24}O_{41}$ shows a higher $\kappa_M$ than $Sr_{14}Cu_{24}O_{41}$ due to the suppressed magnon-hole scattering.[13,14] The room temperature $\kappa$ of $Ca_9La_5Cu_{24}O_{41}$ is found to be ~100 W $m^{-1}$ $K^{-1}$,[14] which is much larger than ~20 W $m^{-1}$ $K^{-1}$ for $Sr_{14}Cu_{24}O_{41}$. Although a lower $\kappa$ of ~50 W $m^{-1}$ $K^{-1}$ has been reported by a different group,[24] $Ca_9La_5Cu_{24}O_{41}$ still has the largest reported $\kappa_M$ at room temperature. As such, this material is promising for innovative thermal management applications by utilizing and controlling magnetic heat transport.[25,26]

Despite the recent investigation of thermal transport in single crystals of cuprates, the effects of defects and grain boundaries on magnon thermal transport are not well understood as compared to phonon transport.[27,28] Grain boundaries act as defects in polycrystalline materials, which scatter phonons and suppress $\kappa_L$. The nanostructuring approach has been used to enhance the figure of merit $ZT$ in thermoelectric materials.[29,30] Regarding the magnon thermal transport, a recent study reported the effects of grain boundaries and defects on magnon thermal transport in textured $Sr_{14}Cu_{24}O_{41}$.[27] The results suggested low transmission coefficients of magnons across grain boundaries. In addition, a four-probe thermal conductivity measurement of the $Sr_{14}Cu_{24}O_{41}$ microrods revealed appreciable magnon thermal transport along the microrod direction, the magnitude of which was correlated to the defect concentration.[31] In comparison to these active studies in $Sr_{14}Cu_{24}O_{41}$, it remains elusive whether the size effects can be observed in magnon and phonon thermal transport in the less hole-doped $Ca_9La_5Cu_{24}O_{41}$. Moreover, localization of magnetic excitations has been predicted in disordered 1D or 2D magnetic systems.[32−35] It has been found that the random disorder can induce the magnon localization that drastically reduces $\kappa_M$. It is interesting to verify whether this localization of magnons can be identified in $Ca_9La_5Cu_{24}O_{41}$ experimentally.

Here, we study the effects of grain size on thermal transport in the spin ladder $Ca_9La_5Cu_{24}O_{41}$. A polycrystalline sample was prepared by consolidating the $Ca_9La_5Cu_{24}O_{41}$ powders by spark plasma sintering (SPS). In comparison, a nanostructured bulk sample was prepared by an additional ball-milling (BM) process before SPS. In addition, a bulk single crystal was grown by the traveling solvent floating zone method. Electron microscopy studies show that the average grain size of the bulk polycrystalline samples is reduced from 4.2 to 0.83 $\mu$m by the additional BM process. The thermal transport measurements of these samples reveal a large suppression of $\kappa_L$ for temperatures ($T$) below about 100 K in the nanostructured sample due to enhanced phonon-boundary scattering. In contrast, the grain size has a negligible effect on magnon thermal transport. The $\kappa_M$ data show a monotonic increase with the temperature, analogous to the $\kappa_M$ in amorphous materials.[36] The mean free paths (MFPs) of magnons and phonons are calculated by analyzing the temperature-dependent $\kappa$ data. The obtained magnon MFPs show weak temperature dependence and are comparable to the lattice constant of the unit cell along the $c$ axis. This finding can be attributed to the disorder-induced magnon localization in polycrystalline $Ca_9La_5Cu_{24}O_{41}$.

## EXPERIMENTAL SECTION

**Material Synthesis.** The $Ca_9La_5Cu_{24}O_{41}$ powder sample was prepared by solid-state reaction (SSR). The starting materials are $CaCO_3$ (purity: 99.5%), $La_2O_3$ (purity: 99.99%), and CuO (purity: 99.7%) powders. These materials were mixed by the molar ratio as Ca/La/Cu = 9:5:24 and heated twice at 1273 K for 24 h in air. The sample was grounded between two heating processes. Subsequently, the obtained powders were ball-milled for 10 h in air using the SPEX SamplePrep-8000M Mixer/Mill. Finally, the ball-milled powders were consolidated into a dense pellet at 1173 K for 5 min under 60 MPa using SPS. For comparison, a pellet was prepared from the powders without ball milling using SPS. The two pellet samples prepared with and without the ball-milling process are denoted as BM and w/o BM, respectively. In addition, a $Ca_9La_5Cu_{24}O_{41}$ single crystal was grown by


https://doi.org/10.1021/acsaelm.1c01164
ACS Appl. Electron. Mater. 2022, 4, 787−794

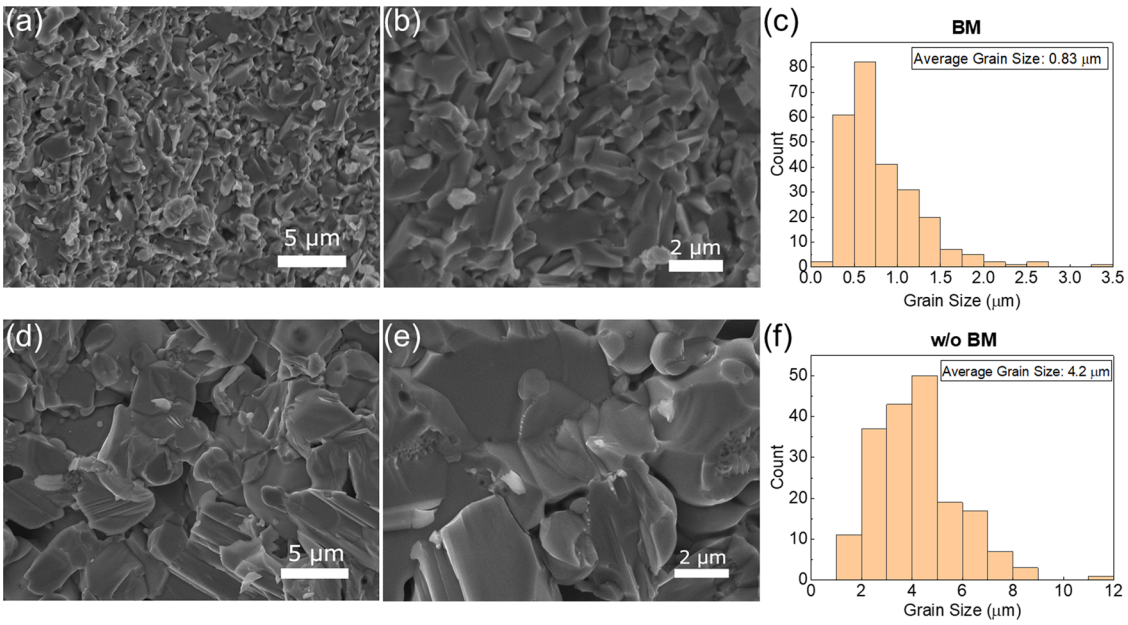


**Figure 2.** SEM images and particle distribution of (a–c) BM sample and (d–f) w/o BM sample.

the traveling solvent floating zone method, and the details of the growth procedure can be found in a prior report.[37]

**Material Characterization.** The phase purity and crystal structure of the samples were characterized using a PANalytical Empyrean Series 2 X-ray diffraction (XRD) machine with Cu K$\alpha$ radiation. The microstructures of the samples were studied by TESCAN Vega3 SBH scanning electron microscopy (SEM). The specific heat ($C$) and thermal conductivity of the samples between 2 and 300 K were measured by the Quantum Design physical property measurement system (PPMS). To study the anisotropic thermal transport properties of the polycrystalline samples, the SPS pellets were cut into bar samples of about 1 × 1 × 6 $mm^3$ along both directions parallel and perpendicular to the SPS press direction. The uncertainty of the thermal conductivity measurement is about 15%.

## RESULTS AND DISCUSSIONS

**Phase and Microstructures.** $Ca_9La_5Cu_{24}O_{41}$ has a layered crystal structure,[38] as shown in Figure 1a. Its unit cell consists of $Cu_2O_3$ ladders and $CuO_2$ chains separated by strings of La/Ca ions. The $Cu_2O_3$ sublattice contains $S$ = 1/2 two-leg spin ladders in the ac plane. The Cu spins interact antiferromagnetically via 180° Cu–O–Cu bonds along the $c$ axis while also antiferromagnetically with its neighboring Cu spin on the same rung within the two-leg ladder. The interaction results in an effective $S$ = 1/2 two-leg model. On the other hand, the $CuO_2$ sublattice contains spin chains with Cu spins interacted by weak ferromagnetic interactions through 90° Cu–O–Cu bonds.[39]

Figure 1b shows the XRD patterns of the samples during various synthesis processes. It can be seen that the $Ca_9La_5Cu_{24}O_{41}$ phase was formed after SSR. All of the major peaks can be indexed as $Ca_9La_5Cu_{24}O_{41}$ (PDF#: 84-1761). A small amount of CuO was observed in the SSR sample. After ball milling, the XRD peaks become broader without the formation of any impurities. The crystallite size of the ball-milled powders before SPS is estimated to be about 46 nm using the Scherrer equation. After SPS, a minor $La_2CaCu_2O_6$ phase was observed. The refinement of the XRD patterns yields the lattice constants of $a \approx 11.31$ Å, $b \approx 12.61$ Å, and $c \approx 27.61$ Å, which are similar to the previous studies.[39,40] The densities of the BM and w/o BM pellets (Figure 1c) are 5.23 and 4.93 g $cm^{-3}$, respectively. The obtained single-crystal $Ca_9La_5Cu_{24}O_{41}$ has a length of about 4 cm and a diameter of about 0.5 cm, as shown in Figure 1d. The crystal quality was checked by XRD and Laue-back reflection, as shown in Figures S1 and S2 in the Supporting Information.

To determine the texture formation on the polycrystalline samples, XRD analysis was also taken on the planes both parallel and perpendicular to the SPS press direction. As shown in Figure S3 of the Supporting Information, the intensity of the (0 0 14) peak is slightly stronger in the parallel direction than that in the perpendicular direction, suggesting the reorientation of the $c$ axis of grains in the pellet plane to a certain extent. However, the texture effect is weak in the obtained $Ca_9La_5Cu_{24}O_{41}$ as compared with a previous study on the textured $Sr_{14}Cu_{24}O_{41}$.[27]

Figure 2 shows the SEM images of the fracture surface of two samples after SPS. The grain size is significantly reduced by ball milling. The grain distribution was determined by the SEM analysis, as displayed in Figure 2c,f. As shown in Figure S4 of the Supporting Information, at least 90 grains are obtained from the SEM image of each sample and are measured in two orthogonal directions to determine the average grain sizes. It is found that the average grain sizes of the BM and w/o BM samples are 0.83 and 4.2 $\mu$m, respectively. For the BM sample, the grain size increases from 46 nm of the powders to 0.83 $\mu$m of the pellet during the SPS process. In addition, as shown in Figure 2d, there are some larger cavities between grains in the w/o BM sample than those in the BM sample. This observation is consistent with the lower density of the w/o BM sample.

**Specific Heat and Thermal Conductivity Measurements.** Figure 3 shows the specific heat data of the BM and w/o BM samples. The grain size has a negligible effect on the specific heat of $Ca_9La_5Cu_{24}O_{41}$. As shown in the inset of Figure 3, a weak peak near 11 K has been observed for both samples, which is consistent with the Néel temperature of about 10 K reported for the $Ca_9La_5Cu_{24}O_{41}$ single crystal.[41] In addition, the specific heat of the two samples at 300 K is about 80% of


https://doi.org/10.1021/acsaelm.1c01164
ACS Appl. Electron. Mater. 2022, 4, 787–794

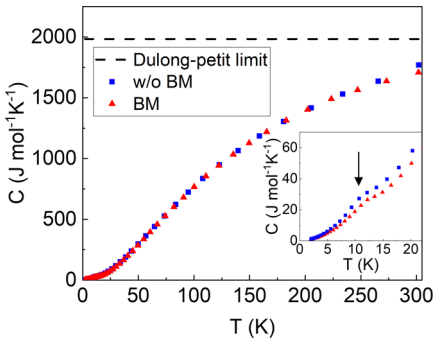


**Figure 3.** Specific heat of the BM and w/o BM samples. The dashed line shows the Dulong–Petit limit of specific heat for $Ca_9La_5Cu_{24}O_{41}$. The inset is the low-temperature specific heat, which shows a hump near 11 K due to the magnetic transition.

the high-temperature specific heat limit based on Dulong–Petit law,[42] which determines the high-temperature specific heat at constant volume $C_v$ as

$$C_v = 3\frac{N}{V}k_B \tag{1}$$

where $N$ is the number of atoms in the unit cell, $V$ is the volume of the unit cell, and $k_B$ is the Boltzmann constant.

Figure 4a shows the $\kappa$ of two $Ca_9La_5Cu_{24}O_{41}$ samples measured perpendicular ($\perp$) and parallel ($\parallel$) to the SPS press direction. The $\kappa$ values of both samples are anisotropic due to the texture effect. Interestingly, the two samples show similar $\kappa$ values for $T > 100$ K, suggesting that the difference in grain size has a negligible effect on thermal transport. Below 100 K, the $\kappa$ of the BM is reduced noticeably as compared with the w/o BM sample. The $\kappa$ along the perpendicular and parallel directions at 40 K are about 2.4 and 1.6 W m$^{-1}$ K$^{-1}$ for the w/o BM sample and 1.7 and 1.3 W m$^{-1}$ K$^{-1}$ for the BM sample, respectively. In addition, the $\kappa$ data for the w/o BM sample shows a clear peak at about 40 K. This peak can be attributed to the phonon contribution as the magnons are not excited at low temperatures due to the energy gap of magnon dispersion. The BM sample, on the other hand, shows a glass-like thermal conductivity, with a monotonic increase of $\kappa$ with the temperature.

**Magnon and Phonon Thermal Transport Analysis.** To correct the effect of porosity ($\Phi$), the solid thermal conductivity ($\kappa_s$) can be calculated as[43]

$$\kappa_s = \kappa\frac{2+\Phi}{2-2\Phi} \tag{2}$$

The porosities are 3.2 and 8.8% for the BM and w/o BM samples, respectively. The calculated $\kappa_s$ of the two samples are shown in Figure 4b together with the single-crystal data along the $c$ axis obtained in this work and reported by Hess et al.[14] and Naruse et al.[24] It should be noted that there is a large difference between the reported $\kappa$ values for $Ca_9La_5Cu_{24}O_{41}$ single crystals. The origin of such a difference is still not clear. Our results of $\kappa$ are closer to the data reported by Naruse et al.[24] in the temperature range of 50–300 K. The $\kappa$ data of the polycrystals are much lower than those of single crystals. Since the thermal transport under 50 K is mainly dominated by phonons, we fit the data below 50 K to the Debye model for three-dimensional phonon transport and extrapolate the fitting results at high temperatures[13]

$$\kappa_L = \frac{k_B}{2\pi^2 v_s}\left(\frac{k_B T}{\hbar}\right)^3 \int_0^{\theta_D/T} \frac{x^4 e^x}{\tau_p^{-1}(e^x-1)^2}dx \tag{3}$$

where $v_s$ is the sound velocity, $\hbar$ is the reduced Planck constant, $\theta_D$ is the Debye temperature, and $x = \frac{\hbar\omega}{k_B T}$. The phonon relaxation time $\tau_p$ can be affected by various scattering processes, including defect scattering, Umklapp scattering, and boundary scattering. According to Matthiessen's rule, $\tau_p$ can be expressed as[44]

$$\tau_p^{-1} = \tau_d^{-1} + \tau_U^{-1} + \tau_b^{-1} = A\omega^4 + Be^{-b/T}T^3\omega^2 + \frac{v_D}{L} \tag{4}$$

where $A$ is the fitting parameter for defect scattering, $B$ and $b$ are the fitting parameters for Umklapp scattering, $v_D$ is the sound velocity, and $L$ is the phonon-boundary scattering MFP.[44]

Figure 4c shows the results of fitting the thermal conductivity to the Debye model. It can be seen that $\kappa_L$ is anisotropic in our samples, due to the texture effect. The BM sample has lower $\kappa_L$ values than the w/o BM sample in both directions below about 100 K. The obtained fitting parameters are listed in Table S1 in the Supporting Information. The values of $L$ change by 1 order of magnitude between two samples, from $(1.3–3.4) \times 10^{-6}$ m for the w/o BM sample to $(1.3–1.4) \times 10^{-7}$ m for the BM sample, which is consistent with the grain sizes estimated by the SEM study. This finding indicates that the boundary scattering is the main cause of the different $\kappa_L$ in two polycrystalline samples.

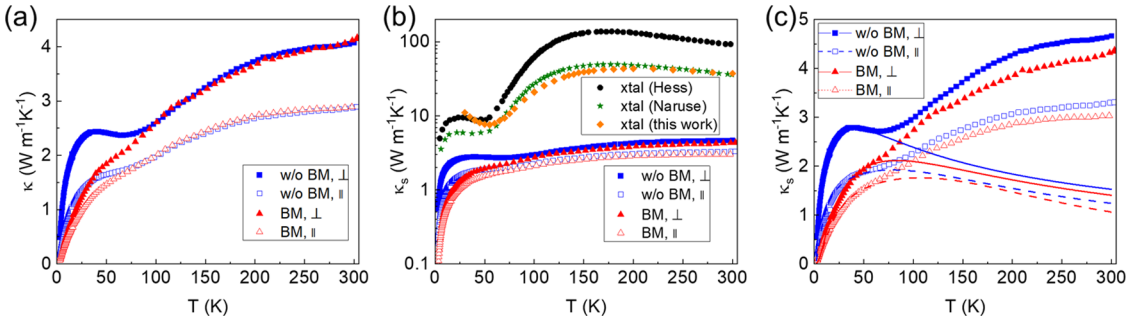


**Figure 4.** (a) Thermal conductivity of the BM and w/o BM samples in both perpendicular ($\perp$) and parallel ($\parallel$) directions. (b) Solid thermal conductivity of the polycrystalline samples in comparison with the single-crystal (xtal) data along the $c$ axis obtained in this work and reported by Naruse et al.[24] and Hess et al.[14] (c) Fits to the low-temperature thermal conductivity with a Debye model for phonon transport.



https://doi.org/10.1021/acsaelm.1c01164
ACS Appl. Electron. Mater. 2022, 4, 787–794

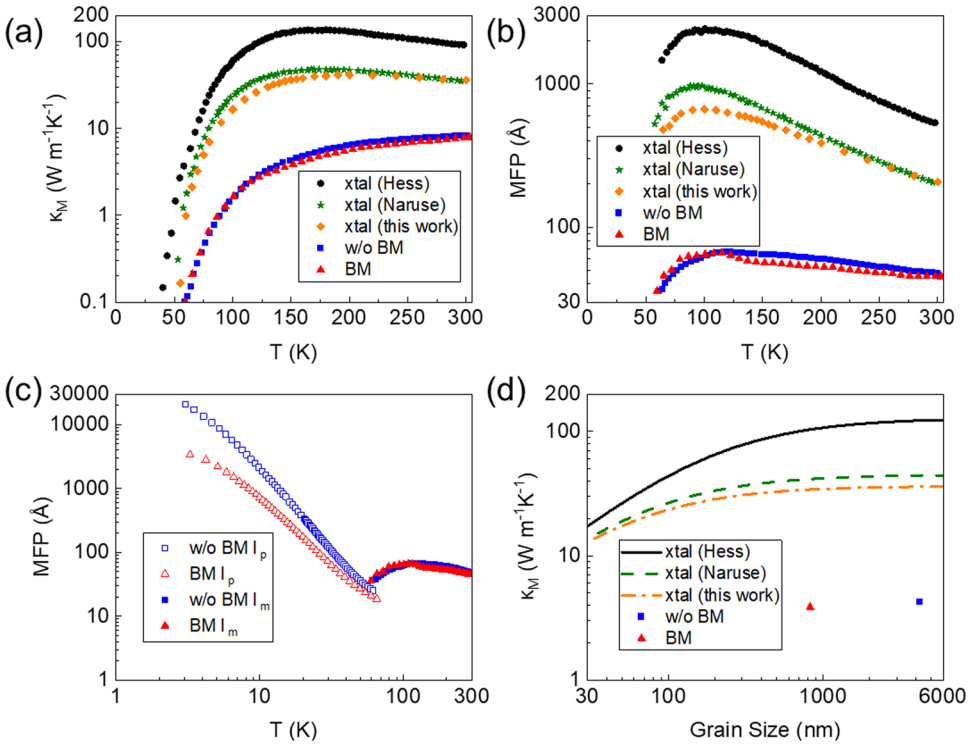


**Figure 5.** (a) Magnon thermal conductivity of the $Ca_9La_5Cu_{24}O_{41}$ polycrystals. Shown for comparison are the magnon thermal conductivity data of single-crystal samples obtained in this work and from the literature.[14,24] (b) Magnon MFPs of polycrystals together with the single-crystal data. (c) Phonon and magnon MFPs of $Ca_9La_5Cu_{24}O_{41}$ polycrystal samples. (d) Calculated and experimental magnon thermal conductivity of $Ca_9La_5Cu_{24}O_{41}$ as a function of grain size at $T$ = 150 K.

The magnon thermal conductivity can be determined by subtracting the lattice contribution from the total thermal conductivity. For the polycrystalline samples, the magnon thermal conductivity can be calculated as $\kappa_M = 2\kappa_{M,\perp} + \kappa_{M,\parallel}$. Figure 5a displays the obtained $\kappa_M$ data of the polycrystals, which increase with the temperature. The $\kappa_M$ at 300 K is about 9 W m$^{-1}$ K$^{-1}$, significantly lower than the single-crystal values of 92 W m$^{-1}$ K$^{-1}$ by Hess et al.,[14] 35 W m$^{-1}$ K$^{-1}$ by Naruse et al.,[24] and 36 W m$^{-1}$ K$^{-1}$ obtained in this work.

To better understand the magnon thermal transport in the polycrystalline samples, we calculate the average magnon mean free path ($l_m$) based on a kinetic model for 1D magnon transport[39]

$$\kappa_M = \frac{3n_s l_m}{\pi\hbar k_B T^2}\int_{\Delta}^{\epsilon_{max}} \frac{\exp\left(\frac{\epsilon}{k_B T}\right)}{\left[\exp\left(\frac{\epsilon}{k_B T}\right)+3\right]^2}\epsilon^2 d\epsilon \quad (5)$$

where $n_s$ is the number of ladders per unit cross sectional area perpendicular to ladders, $\Delta$ is the energy gap of the singlet−triplet dispersion of ladders, and $\epsilon_{max}$ is the band maximum of the spin excitations of ladders. In the analysis, the values of $\Delta$ and $\epsilon_{max}$ are chosen to be 32.5 and 200 meV, which are obtained from a previous inelastic neutron scattering study.[45] Figure 5b shows the calculated $l_m$ of the polycrystalline samples in comparison with the single-crystal data. The $l_m$ of the $Ca_9La_5Cu_{24}O_{41}$ single crystals along the $c$ axis are very large, about 660−2300 Å at 100 K and 200−500 Å at 300 K. For the polycrystalline samples, $l_m$ is highly suppressed, with only about 65 Å at 100 K and 50 Å at 300 K. The two polycrystalline samples show similar $l_m$ values despite different grain sizes. In addition, the temperature dependence of $l_m$ for the polycrystalline samples is much weakened as compared with single crystals.

To investigate the size effects on phonon thermal transport, we calculate the average phonon MFP $l_p$ according to the Debye model as[46]

$$l_p = \kappa_{s,L}\left(\frac{k_B{}^4 T^3}{2\pi^2 v_s^2 \hbar^3}\int_0^{\theta_D/T}\frac{x^4 e^x}{(e^x-1)^2}dx\right)^{-1} \quad (6)$$

where $\kappa_{s,L}$ and $v_s$ are the solid lattice thermal conductivity and sound velocity of phonons, respectively. The $\kappa_{s,L}$ is calculated as $\kappa_{s,L} = (2\kappa_{s,L,\perp} + \kappa_{s,L,\parallel})/3$. The calculated $l_p$ data below 60 K are shown in Figure 5c together with the obtained $l_m$. The $l_p$ data for both samples decrease with the increasing temperature. The maximum values of $l_p$ are about 2.1 $\mu$m for the w/o BM sample and 330 nm for the BM sample, which are consistent with the average grain sizes estimated from SEM images. Both diffusive phonon-boundary scattering and phonon-point defect scattering can reduce $l_p$. The Rayleigh scattering cross section of atomic defects decreases with the increasing phonon wavelength ($\lambda$) according to $\lambda^{-4}$. Thus, phonon transport is dominated by phonon-boundary scattering in the low-temperature limit, where only long-$\lambda$, low-frequency phonons are populated. Therefore, the reduced $l_p$ in the BM sample is mainly attributed to the enhanced boundary scattering.

In order to better understand the origin of the suppressed $\kappa_M$ and $l_m$ in the polycrystalline samples, we calculate the magnon thermal conductivity with eq 5 by including a magnon-boundary scattering MFP ($l_b$) in the total MFP as


https://doi.org/10.1021/acsaelm.1c01164
ACS Appl. Electron. Mater. 2022, 4, 787−794

$$l_m^{-1} = l_{xtal}^{-1} + l_b^{-1} \quad (7)$$

where $l_{xtal}$ is the magnon MFP of the single crystal. As shown in Figure 5d, the experimental $\kappa_M$ data are much lower than the calculated results without additional defect scattering. Even considering the boundary scattering MFP as 30 nm, the predicted $\kappa_M$ is still larger than the measurement results. The large difference between the calculated and experimental $\kappa_M$ suggests that the magnon thermal transport in the polycrystals is dominated by defect scattering. Previous work has revealed the presence of various defects, including edge dislocations and planer defects, in the $Sr_{14}Cu_{24}O_{41}$ polycrystals synthesized by SSR followed by SPS.[27] The formation of these defects could be attributed to mass diffusion during SSR or mechanical deformation during SPS. As such, these defects are also expected to be present in our $Ca_9La_5Cu_{24}O_{41}$ samples, which were prepared using a similar method. Furthermore, owing to a large difference in the atomic radius of Ca and La, a large lattice distortion can be introduced to the materials by atomic substitution in the $Ca_9La_5Cu_{24}O_{41}$ samples. Actually, the atomic arrangement in both spin ladder and chain planes is disordered according to the XRD study.[38] These atomic disorders combined with various defects can significantly scatter magnon thermal transport. As such, the obtained $l_m$ value near 100 K is about 65 Å, which is comparable to the lattice parameter of the unit cell along the $c$ axis (~28 Å). This result suggests the possible localization of magnons in the polycrystalline samples. Magnons are strongly damped by defects and disorders so that the magnon thermal transport is approaching the Ioffe−Regel limit.[47] Since two polycrystalline samples with different grain sizes show similar $l_m$, the localization of magnons can be mainly attributed to the scattering by defects inside the grains instead of scattering at grain boundaries.

Sologubenko et al. studied magnetic thermal transport in another spin ladder compound $(C_5H_{12}N)_2CuBr_4$.[48] It has been found that strong backscattering by impurities or disorders combined with a low probability of interladder transfer may lead to a localization of magnetic excitations. Such a localization requires that the following condition

$$\frac{v_m^{\perp}}{c} < \frac{v_m^{\parallel}}{d_{def}} \quad (8)$$

should be satisfied, where $v_m^{\perp}$ and $v_m^{\parallel}$ are the characteristic velocities of magnetic excitations perpendicular and parallel to the ladder direction, $c$ is the lattice constant, and $d_{def}$ is the average distance between the defects. Since the magnon velocity is proportional to the spin−spin coupling energy $J$,[39] we have $v_m^{\perp}/v_m^{\parallel} \approx J^{\perp}/J^{\parallel} = 1/130$ according to the reported $J$ values of $(Sr,Ca,La)_{14}Cu_{24}O_{41}$.[20,23] Assuming that the $d_{def}$ is of the order of the $l_m$, the above condition (eq 8) can be satisfied. This result also suggests the possible magnon localization in our polycrystalline samples.

## CONCLUSIONS

Polycrystalline $Ca_9La_5Cu_{24}O_{41}$ samples have been prepared by consolidating the powders by SPS. It has been found that the additional BM process before SPS can significantly reduce the average grain size from about 4.2 to 0.83 $\mu$m in the obtained bulk samples. The size effects can be observed in phonon thermal transport, which leads to a suppressed $\kappa_L$ and phonon MFPs below about 100 K. On the other hand, reducing grain size has little influence on magnon thermal transport. The $\kappa_M$ of the polycrystals is suppressed remarkably as compared to bulk single crystals. The thermal transport analysis suggests that the suppressed $\kappa_M$ is mainly attributed to magnon-defect scattering, instead of magnon-boundary scattering. The magnon MFP is found to be about 65 Å near 100 K, which is comparable to the lattice constant of the unit cell along the $c$ axis. The magnons in the polycrystalline samples are strongly damped by defects, suggesting possible magnon localization under the Ioffe−Regel criterion. These findings offer useful insights into magnon thermal transport in defected polycrystalline materials. The localization of magnons could be utilized for thermal management applications, such as thermal switches.

## ASSOCIATED CONTENT

### Supporting Information

The Supporting Information is available free of charge at https://pubs.acs.org/doi/10.1021/acsaelm.1c01164.

Additional XRD results of the $Ca_9La_5Cu_{24}O_{41}$ samples, Laue-back refection pattern, grain size analysis, and fitting parameters of the Debye model (PDF)

## AUTHOR INFORMATION


### Corresponding Author

**Xi Chen** − *Department of Electrical and Computer Engineering, University of California, Riverside, California 92521, United States;* orcid.org/0000-0003-4251-7035; Email: xichen@ucr.edu

### Authors

**Shuchen Li** − *Department of Electrical and Computer Engineering, University of California, Riverside, California 92521, United States*

**Shucheng Guo** − *Department of Electrical and Computer Engineering, University of California, Riverside, California 92521, United States*

**Youming Xu** − *Department of Electrical and Computer Engineering, University of California, Riverside, California 92521, United States*

**Jianshi Zhou** − *Materials Science and Engineering Program, Texas Materials Institute, The University of Texas at Austin, Austin, Texas 78712, United States;* orcid.org/0000-0002-7667-5640

Complete contact information is available at: https://pubs.acs.org/10.1021/acsaelm.1c01164


### Author Contributions

[§]S.L. and S.G. contributed equally to this work.

### Notes

The authors declare no competing financial interest.

## ACKNOWLEDGMENTS

This work was supported by the start-up funds from the University of California, Riverside. J.Z. was supported by the National Science Foundation through the Center for Dynamics and Control of Materials: an NSF MRSEC under Cooperative Agreement No. DMR-1720595.

## REFERENCES

(1) Moore, A. L.; Shi, L. Emerging challenges and materials for thermal management of electronics. *Mater. Today* **2014**, *17*, 163−174.

(2) Liu, Z.; Yang, X.; Zhang, B.; Li, W. High Thermal Conductivity of Wurtzite Boron Arsenide Predicted by Including Four-Phonon Scattering with Machine Learning Potential. *ACS Appl. Mater. Interfaces* **2021**, *13*, 53409−53415.
(3) Pan, G.; Yao, Y.; Zeng, X.; Sun, J.; Hu, J.; Sun, R.; Xu, J.-B.; Wong, C.-P. Learning from Natural Nacre: Constructing Layered Polymer Composites with High Thermal Conductivity. *ACS Appl. Mater. Interfaces* **2017**, *9*, 33001−33010.
(4) Klemens, P. G.; Williams, R. K. Thermal conductivity of metals and alloys. *Int. Mater. Rev.* **1986**, *31*, 197−215.
(5) Berman, R.; Simon, F. E.; Wilks, J. Thermal Conductivity of Dielectric Crystals: The 'Umklapp' Process. *Nature* **1951**, *168*, 277−280.
(6) Kang, J. S.; Li, M.; Wu, H.; Nguyen, H.; Hu, Y. Experimental observation of high thermal conductivity in boron arsenide. *Science* **2018**, *361*, 575−578.
(7) Li, S.; Zheng, Q.; Lv, Y.; Liu, X.; Wang, X.; Huang, P. Y.; Cahill, D. G.; Lv, B. High thermal conductivity in cubic boron arsenide crystals. *Science* **2018**, *361*, 579−581.
(8) Tian, F.; Song, B.; Chen, X.; Ravichandran, N.; Lv, Y.; Chen, K.; Sullivan, S.; Kim, J.; Zhou, Y.; Liu, T.-H.; Goni, M.; Ding, Z.; Sun, J.; Gamage, U. G. G. A.; Sun, H.; Ziyaee, H.; Huyan, S.; Deng, L.; Zhou, J.; Schmidt, A. J.; Chen, S.; Chu, C.-W.; Huang, P. Y.; Broido, D.; Li, S.; Chen, G.; Ren, Z. Unusual high thermal conductivity in boron arsenide bulk crystals. *Science* **2018**, *361*, 582−585.
(9) Fröhlich, H.; Heitler, W. Time effects in the magnetic cooling method II—the conductivity of heat. *Proc. R. Soc. London, Ser. A* **1936**, *155*, 640−652.
(10) Lüthi, B. Thermal conductivity of yttrium iron garnet. *J. Phys. Chem. Solids* **1962**, *23*, 35−38.
(11) Zotos, X.; Naef, F.; Prelovsek, P. Transport and conservation laws. *Phys. Rev. B* **1997**, *55*, 11029−11032.
(12) Kudo, K.; Ishikawa, S.; Noji, T.; Adachi, T.; Koike, Y.; Maki, K.; Tsuji, S.; Kumagai, K. Spin Gap and Hole Pairing of $Sr_{14-x}A_xCu_{24}O_{41}$(A = Ca and La) Single Crystals Studied by the Electrical Resistivity and Thermal Conductivity. *J. Low Temp. Phys.* **1999**, *117*, 1689−1693.
(13) Sologubenko, A. V.; Giannó, K.; Ott, H. R.; Ammerahl, U.; Revcolevschi, A. Thermal Conductivity of the Hole-Doped Spin Ladder System $Sr_{14-x}Ca_xCu_{24}O_{41}$. *Phys. Rev. Lett.* **2000**, *84*, 2714−2717.
(14) Hess, C.; Baumann, C.; Ammerahl, U.; Büchner, B.; Heidrich-Meisner, F.; Brenig, W.; Revcolevschi, A. Magnon heat transport in $(Sr,Ca,La)_{14}Cu_{24}O_{41}$. *Phys. Rev. B* **2001**, *64*, No. 184305.
(15) Chen, X.; Carrete, J.; Sullivan, S.; van Roekeghem, A.; Li, Z.; Li, X.; Zhou, J.; Mingo, N.; Shi, L. Coupling of Spinons with Defects and Phonons in the Spin Chain Compound $Ca_2CuO_3$. *Phys. Rev. Lett.* **2019**, *122*, No. 185901.
(16) Sologubenko, A. V.; Giannò, K.; Ott, H. R.; Vietkine, A.; Revcolevschi, A. Heat transport by lattice and spin excitations in the spin-chain compounds $SrCuO_2$ and $Sr_2CuO_3$. *Phys. Rev. B* **2001**, *64*, No. 054412.
(17) Morelli, D. T.; Heremans, J.; Doll, G.; Picone, P. J.; Jenssen, H. P.; Dresselhaus, M. S. Thermal properties of single-crystal $La_2CuO_{4-\delta}$. *Phys. Rev. B* **1989**, *39*, 804−807.
(18) Notbohm, S.; Ribeiro, P.; Lake, B.; Tennant, D. A.; Schmidt, K. P.; Uhrig, G. S.; Hess, C.; Klingeler, R.; Behr, G.; Büchner, B.; Reehuis, M.; Bewley, R. I.; Frost, C. D.; Manuel, P.; Eccleston, R. S. One- and Two-Triplon Spectra of a Cuprate Ladder. *Phys. Rev. Lett.* **2007**, *98*, No. 27403.
(19) Chen, X.; Bansal, D.; Sullivan, S.; Abernathy, D. L.; Aczel, A. A.; Zhou, J.; Delaire, O.; Shi, L. Weak coupling of pseudoacoustic phonons and magnon dynamics in the incommensurate spin-ladder compound $Sr_{14}Cu_{24}O_{41}$. *Phys. Rev. B* **2016**, *94*, No. 134309.
(20) Osafune, T.; Motoyama, N.; Eisaki, H.; Uchida, S. Optical Study of the $Sr_{14-x}Ca_xCu_{24}O_{41}$ System: Evidence for Hole-Doped $Cu_2O_3$ Ladders. *Phys. Rev. Lett.* **1997**, *78*, 1980−1983.
(21) Wang, J.; Lin, Y.; Zou, H.; Pu, S.; Shi, J. Structural transition, electrical and magnetic properties of the B-site Co doped $Sr_{14}Cu_{24}O_{41}$ compounds. *J. Phys.: Condens. Matter* **2009**, *21*, No. 075601.
(22) Nücker, N.; Merz, M.; Kuntscher, C. A.; Gerhold, S.; Schuppler, S.; Neudert, R.; Golden, M. S.; Fink, J.; Schild, D.; Stadler, S.; Chakarian, V.; Freeland, J.; Idzerda, Y. U.; Conder, K.; Uehara, M.; Nagata, T.; Goto, J.; Akimitsu, J.; Motoyama, N.; Eisaki, H.; Uchida, S.; Ammerahl, U.; Revcolevschi, A. Hole distribution in $(Sr,Ca,Y,La)_{14}Cu_{24}O_{41}$ ladder compounds studied by x-ray absorption spectroscopy. *Phys. Rev. B* **2000**, *62*, 14384−14392.
(23) Vuleticc, T.; Korin-Hamzicc, B.; Ivek, T.; Tomic, S.; Gorshunov, B.; Dressel, M.; Akimitsu, J. The spin-ladder and spin-chain system $(La,Y,Sr,Ca)_{14}Cu_{24}O_{41}$: Electronic phases, charge and spin dynamics. *Phys. Rep.* **2006**, *428*, 169−258.
(24) Naruse, K.; Kawamata, T.; Ohno, M.; Matsuoka, Y.; Kumagai, K.; Koike, Y. Thermal conductivity due to magnons in high-quality single crystals of the two-leg spin-ladder system $(Ca,Sr,La)_{14}Cu_{24}O_{41}$. *Solid State Commun.* **2013**, *154*, 60−63.
(25) Terakado, N.; Nara, Y.; Machida, Y.; Takahashi, Y.; Fujiwara, T. Dynamic control of heat flow using a spin-chain ladder cuprate film and an ionic liquid. *Sci. Rep.* **2020**, *10*, No. 14468.
(26) Otter, M.; Athanasopoulos, G.; Hlubek, N.; Montagnese, M.; Labois, M.; Fishman, D. A.; de Haan, F.; Singh, S.; Lakehal, D.; Giapintzakis, J.; Hess, C.; Revcolevschi, A.; van Loosdrecht, P. H. M. Optical probing of anisotropic heat transport in the quantum spin ladder $Ca_9La_5Cu_{24}O_{41}$. *Int. J. Heat Mass Transfer* **2012**, *55*, 2531−2538.
(27) Chen, X.; Jarvis, K.; Sullivan, S.; Li, Y.; Zhou, J.; Shi, L. Effects of grain boundaries and defects on anisotropic magnon transport in textured $Sr_{14}Cu_{24}O_{41}$. *Phys. Rev. B* **2017**, *95*, No. 144310.
(28) Wang, Z.; Alaniz, J. E.; Jang, W.; Garay, J. E.; Dames, C. Thermal Conductivity of Nanocrystalline Silicon: Importance of Grain Size and Frequency-Dependent Mean Free Paths. *Nano Lett.* **2011**, *11*, 2206−2213.
(29) Poudel, B.; Hao, Q.; Ma, Y.; Lan, Y.; Minnich, A.; Yu, B.; Yan, X.; Wang, D.; Muto, A.; Vashaee, D.; Chen, X.; Liu, J.; Dresselhaus, M. S.; Chen, G.; Ren, Z. High-Thermoelectric Performance of Nanostructured Bismuth Antimony Telluride Bulk Alloys. *Science* **2008**, *320*, 634−638.
(30) Biswas, K.; He, J.; Blum, I. D.; Wu, C.-I.; Hogan, T. P.; Seidman, D. N.; Dravid, V. P.; Kanatzidis, M. G. High-performance bulk thermoelectrics with all-scale hierarchical architectures. *Nature* **2012**, *489*, 414−418.
(31) Chen, X.; Kim, J.; Jia, Q.; Sullivan, S. E.; Xu, Y.; Jarvis, K.; Zhou, J.; Shi, L. Synthesis and Magnon Thermal Transport Properties of Spin Ladder $Sr_{14}Cu_{24}O_{41}$ Microstructures. *Adv. Funct. Mater.* **2020**, *30*, No. 2001637.
(32) Doty, C. A.; Fisher, D. S. Effects of quenched disorder on spin-1/2 quantum XXZ chains. *Phys. Rev. B* **1992**, *45*, 2167−2179.
(33) Arakawa, N.; Ohe, J. I. Weak localization of magnons in a disordered two-dimensional antiferromagnet. *Phys. Rev. B* **2018**, *97*, No. 020407.
(34) Arakawa, N.; Ohe, J. I. Inplane anisotropy of longitudinal thermal conductivities and weak localization of magnons in a disordered spiral magnet. *Phys. Rev. B* **2018**, *98*, No. 014421.
(35) Jenčič, B.; Prelovšek, P. Spin and thermal conductivity in a classical disordered spin chain. *Phys. Rev. B* **2015**, *92*, No. 134305.
(36) Slack, G. A. The Thermal Conductivity of Nonmetallic Crystals. In *Solid State Physics*; Academic Press, 1979; Vol. *34*, pp 1−71.
(37) Revcolevschi, A.; Ammerahl, U.; Dhalenne, G. Crystal growth of pure and substituted low-dimensionality cuprates $CuGeO_3$, $La_2CuO_4$, $SrCuO_2$, $Sr_2CuO_3$ and $Sr_{14}Cu_{24}O_{41}$ by the floating zone and travelling solvent zone methods. *J. Cryst. Growth* **1999**, *198*−*199*, 593−599.
(38) Siegrist, T.; Schneemeyer, L. F.; Sunshine, S. A.; Waszczak, J. V.; Roth, R. S. A new layered cuprate structure-type, $(A_{1-x}A'_x)_{14}Cu_{24}O_{41}$. *Mater. Res. Bull.* **1988**, *23*, 1429−1438.


https://doi.org/10.1021/acsaelm.1c01164
ACS Appl. Electron. Mater. 2022, 4, 787−794

(39) Hess, C. Heat transport of cuprate-based low-dimensional quantum magnets with strong exchange coupling. *Phys. Rep.* **2019**, *811*, 1−38.
(40) Matsuda, M.; Kojima, K. M.; Uemura, Y. J.; Zarestky, J. L.; Nakajima, K.; Kakurai, K.; Yokoo, T.; Shapiro, S. M.; Shirane, G. Ordering of oxygen moments in ferromagnetic edge-sharing $CuO_4$ chains in $La_{14-x}Ca_xCu_{24}O_{41}$. *Phys. Rev. B* **1998**, *57*, 11467−11471.
(41) Ammerahl, U.; Büchner, B.; Kerpen, C.; Gross, R.; Revcolevschi, A. Ising-like antiferromagnetism in $Ca_9La_5Cu_{24}O_{41}$. *Phys. Rev. B* **2000**, *62*, R3592−R3595.
(42) Dulong, P. L.; Petit, A.-T. Recherches sur quelques points importans de la theorie de la chaleur. *Ann. Chim. Phys.* **1819**, *10*, 395−413.
(43) Takashiri, M.; Tanaka, S.; Hagino, H.; Miyazaki, K. Combined effect of nanoscale grain size and porosity on lattice thermal conductivity of bismuth-telluride-based bulk alloys. *J. Appl. Phys.* **2012**, *112*, No. 084315.
(44) Callaway, J. Model for Lattice Thermal Conductivity at Low Temperatures. *Phys. Rev.* **1959**, *113*, 1046−1051.
(45) Eccleston, R. S.; Uehara, M.; Akimitsu, J.; Eisaki, H.; Motoyama, N.; Uchida, S. Spin Dynamics of the Spin-Ladder Dimer-Chain Material $Sr_{14}Cu_{24}O_{41}$. *Phys. Rev. Lett.* **1998**, *81*, 1702−1705.
(46) Chen, X.; Weathers, A.; Moore, A.; Zhou, J.; Shi, L. Thermoelectric Properties of Cold-Pressed Higher Manganese Silicides for Waste Heat Recovery. *J. Electron. Mater.* **2012**, *41*, 1564−1572.
(47) Ioffe, A. F.; Regel, A. R. Non-crystalline, amorphous and liquid electronic semiconductors. *Prog. Semicond.* **1960**, *4*, 237−291.
(48) Sologubenko, A. V.; Lorenz, T.; Mydosh, J. A.; Thielemann, B.; Rønnow, H. M.; Rüegg, C.; Krämer, K. W. Evidence for spinon localization in the heat transport of the spin-1/2 ladder compound $(C_5H_{12}N)_2CuBr_4$. *Phys. Rev. B* **2009**, *80*, No. 220411.





https://doi.org/10.1021/acsaelm.1c01164
*ACS Appl. Electron. Mater.* 2022, 4, 787−794